Component Separation for Spectral X-Ray Imaging Using the XPAD3 Hybrid Pixel Camera

M. Dupont, Y. Boursier, A. Bonissent, F. Galland, F. Cassol Brunner, C. Morel

Component Separation for Spectral X-ray Imaging using the Hybrid Pixel Camera XPAD3

M. Dupont, Y. Boursier, A. Bonissent, F. Cassol, C. Kronland-Martinet, and C. Morel, *Member, IEEE*

***Abstract*—Hybrid pixel cameras are new devices for which photon counting replaces charge integration, which have the capability to acquire spectral information on the counted photons. This ability is of uppermost importance for the development of new polychromatic X-ray imaging for which one goal is to separate images in several components of physical and biological interest. For instance, the photoelectric and Compton contributions can be separated while several contrast agents can be simultaneously localized. In this paper, we investigate the capability to perform component separation by using the newly developed hybrid pixel camera XPAD3 incorporated in the microCT demonstrator PIXSCAN. Several experiments have been led on data simulated analytically and by Monte Carlo, showing the great interest of component separation to enhance the contrast of materials when compared to classical X-ray data processing in microCT, and to cancel beam hardening artifacts. Results obtained on real data acquired with PIXSCAN on a phantom including Aluminium, water and Yttrium, the latter being treated as a contrast agent, show that the photoelectric, Compton and Yttrium components can be clearly separated and that each of them carries information allowing for the identification of different structures within the phantom.**

I. Introduction

The advent of hybrid pixel detectors in X-ray imaging opens the way to the acquisition of spectral data. These new devices, for which photon counting replaces charge integration, incorporate a dedicated readout electronic for each pixel that can select energies by using a parametrizable energy threshold. This ability is of uppermost importance for the development of new X-ray imaging approaches that will exploit spectral information on the detected X-rays. Spectral measurements in X-ray imaging pave the way to the separation of images in several components of physical and biological interest: the photoelectric and Compton contributions can be separated as well as several contrast agents can be simultaneously localized. This idea of material decomposition was early proposed in 1976 ([1]), but one had to wait for the advent of pre-clinical or clinical systems based on energy discriminating detectors to implement it on real measurements ([2]). The hybrid pixel camera XPAD3 was developed and characterized at CPPM ([4], [5]) and incorporated in the micro-CT demonstrator PIXSCAN ([6]). It has been proven that spectral measurements acquired with the camera XPAD3 have permitted to realize subtractive K-edge imaging on phantoms with two contrast agents ([7]). This approach however suffers from high noise level of the low statistics within narrow energy ranges around K-edge values resulting from the subtraction between two acquisitions with only one energy threshold.

M. Dupont, Y. Boursier, A. Bonissent, F. Cassol, C. Kronland-Martinet, and C. Morel are with CPPM, Aix-Marseille Université, CNRS/IN2P3, Marseille, France.

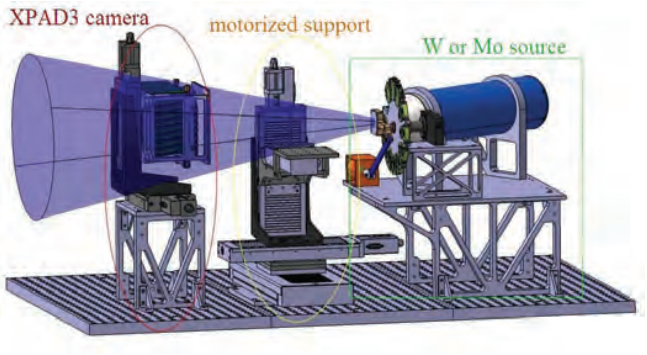

Figure 1: Layout of the microCT demonstrator PIXSCAN.

In this paper, we investigate the component separation approach with the camera XPAD3 in order to overcome these limits of subtractive K-edge imaging. We first describe the microCT imaging system PIXSCAN and then introduce the general framework for component separation with spectral measurements based on the camera XPAD3. We focus on the separation problem with two components, namely the photoelectric and Compton components. We show that such a separation on noisy simulated data with an optimized setup i) enhances the contrast and the Contrast-to-Noise Ratio (CNR) between biological materials (adipose, soft tissues) and water, and ii) reduces beam hardening artifacts that may strongly degrade image quality. Finally, we extend the previous separation problem with a third component treated as a contrast agent depicted by its K-edge value, in our case Yttrium. We demonstrate on real data acquired with the camera XPAD3 that the photoelectric, Compton and Yttrium components can be clearly separated and that different structures of the imaged objet can be identified.

II. The PIXSCAN imaging system

PIXSCAN (see Figure 1) is a microCT demonstrator constituted in three parts : i) a detector holder equipped with the hybrid pixel camera XPAD3; ii) a rotating animal holder; iii) a X ray source holder with a rotating filter wheel comprising eight slots.

Two X-ray sources with two different anodes are available on PIXSCAN and can be easily interchanged : the RTW Molybden anode tube (MCBM 65B-50 Mo, RTW, Berlin, Germany) and the UltraBright Tungsten anode tube (UltraBright Microfocus W(96004), Oxford Instruments, Scotts Valley,

978-1-4799-0534-8/13/$31.00 ©2013 IEEE

USA). Both of them provide emission spot sizes not larger than $(50 \times 50)\ \mu m^2$ and a wide aperture of $20°$ and $33°$ for the Mo and W anodes, respectively. A Tungsten spectrum is displayed as an example on Figure 2 together with its filtration by an Yttrium filter.

The imaged object is placed on a rotating plate between the detector and the fixed X-ray source with a magnification ranging from 1.6 to 2.7, according to the geometrical configuration set by the user. The motorized animal support from Newport (M-MTM150CC.1 Linear Stage) provides translation motions in 3 directions with 5 μm accuracy and one rotation around a vertical axis with $0.1°$ angular steps.

The hybrid pixel camera XPAD3 ([3]) consists of chips XPAD3-2([4]) bump bonded to 500 μm thick Silicon sensors to form horizontal modules. Eight modules of 7 chips of 80×120 pixels are tiled vertically to form an overall sensitive surface of $(8 \times 11)\ cm^2$ composed of more than $500,000$ square pixels of $(130 \times 130)\ \mu m^2$. The counting rate is up to 10^6 counts/pixel/second and a fast detector readout allows to acquire full frames at a speed up to 500 images/second.

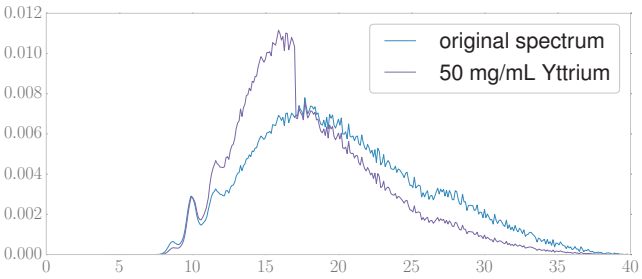

Figure 2: Modification of a Tungsten energy spectrum by Yttrium filtration. The W spectrum was obtained with a 40 kVp voltage. Yttrium has a K-edge value of 17 keV. Both spectra are normalized according to their integral.

III. Component separation method

A. Polychromatic acquisition model

Let us assume that the measurement of each pixel i of a X-ray camera is corrupted by a photon noise modeled as a Poisson noise. The generic framework for polychromatic CT is based on the acquisition model $I^i_{(\alpha,\beta)} = \mathcal{P}\left(m^i_{(\alpha,\beta)}\right)$ with:

$$m^i_{(\alpha,\beta)} = \int_{\alpha}^{+\infty} I^0_\beta(E)\eta^i(E)\exp\left(-\int_{\mathcal{L}_i}\mu(E,l)dl\right)dE \quad (1)$$

and where i) I^i is the number of photons counted by the pixel i; ii) α is the threshold of the pixel i that can be controlled by the user and set up before acquisition. All photons carrying a lower energy than α will not be counted; iii) $I^0_\beta(E)$ stands for the emitted spectrum of the source modulated by a transmission function $g_\beta(E)$ of a filter placed at the output of the source, such that $I^0_\beta = I^0(E)g_\beta(E)$. $I^0_\beta(E)$ is expressed as a number of photons per energy unit per pixel. For the sake of simplicity, we assume that $I^0_\beta(E)$ is the same for all the pixels, *i.e.* we neglect the spatial variations of intensity of the emitted spectrum; iv) $\eta^i(E)$ is the efficiency of the pixel i supposed to be known after a calibration procedure; v) $\mu(E,l)$ is the unknown linear attenuation coefficient distribution map at energy E. It is integrated along the geometric line-of-sight $\mathcal{L}_i$ corresponding to the pixel i; vi) $y = \mathcal{P}(\lambda)$ stands for a realization of a Poisson noise of parameter λ.

We make the assumption that $\mu(E,l)$ can be expressed as a linear combination of K components of interests $\mu(E,l) = \sum_{k=1}^{K} c_k(l)\mu_k(E)$. In the previous expression, each energy-dependent function $\mu_k(E)$ is known and injected in the component separation problem. It may for instance represent a model of a physical process like the photoelectric effect or the linear attenuation coefficient of a material k, typically a contrast agent.

If we denote $a^i_k = \int_{\mathcal{L}_i} c_k(l)dl$, Eq. 1 writes,

$$m^i_{(\alpha,\beta)} = \int_{\alpha}^{+\infty} I^0_\beta(E)\eta^i(E)\exp\left(-\sum_{k=1}^{K} a^i_k\mu_k(E)\right)dE$$

The separation of K components $\{a_k\}_{k=1...K}$ is directly processed pixelwise on cone-beam projections from a set of $N \geq K$ distinct acquisitions $\{I_{(\alpha_j,\beta_j)}\}_{j=1...N}$ obtained with different configurations of the experimental setup, i.e. different values of (α,β). The energy threshold of pixels and the shape of the emitted spectrum are indeed the parameters of importance that provide discriminating spectral information.

Assuming that a Poisson noise of parameter $m^i_{(\alpha,\beta)}$ is well approximated by a Gaussian noise of mean $m^i_{(\alpha,\beta)}$ and of variance $m^i_{(\alpha,\beta)}$ at high statistics (*i.e.* typically when $m^i_{(\alpha,\beta)} >> 100$), we solve for each pixel i the following minimization problem:

$$\hat{\mathbf{a}}^\mathbf{i} = \arg\min_{\mathbf{a}^\mathbf{i}\in\mathcal{C}} \|\mathbf{I}^\mathbf{i} - \mathbf{m}^\mathbf{i}(\mathbf{a}^\mathbf{i})\|^\mathbf{2} \quad (2)$$

where $\mathbf{a}^\mathbf{i} = [a^i_1, a^i_2, \cdots, a^i_K] \in \mathbb{R}^K$, $\mathcal{C}$ is the positive convex set, i.e. $\mathcal{C} = \{\mathbf{a} \in \mathbb{R}^K, a_k \geq 0, k = 1...K\}$, and if we adopt for simplicity the notations $I^i_{(\alpha_j,\beta_j)} = I^i_j$ and $m^i_{(\alpha_j,\beta_j)} = m^i_j$, then $\mathbf{I}^\mathbf{i} = [I^i_1, I^i_2, \cdots, I^i_N]$ and $\mathbf{m}^\mathbf{i} = [m^i_1, m^i_2, \cdots, m^i_N]$ with $\mathbf{I}^\mathbf{i}, \mathbf{m}^\mathbf{i} \in \mathbb{R}^N$. The estimation of the K components of interest $\{a_k\}_{k=1...K}$ is then expressed as a minimization problem which encompasses priors on the components to estimate, e.g. here a positivity prior.

For each experience presented in the following, we used the numerical minimization program MINUIT2[1] to solve the non-linear least square problem.

IV. Results and discussion

A. Contrast enhancement

One of the aims of spectral CT is to increase contrast between soft tissues. We show here that we can achieve this aim by inspecting the photoelectric contribution. Indeed, the photoelectric cross section depends on the atomic number Z of materials and is responsible for most of contrast in microCT images whereas the Compton cross section only depends on density, thus playing almost no role on contrast. Moreover,

[1] http://root.cern.ch/root/html/MATH_MINUIT2_Index.html

it is well known that the diffusion process induced by the Compton effect triggers off a degradation of microCT images, which results in a loss of contrast. In this study, we choose $K = N = 2$, and focused on the separation of physical processes, i.e. the photoelectric contribution noted $a_1 = a_{ph}$ with $\mu_{ph}(E) = 1/E^3$ and the Compton contribution noted $a_2 = a_C$ with $\mu_C(E)$ deduced from a polynomial fit of order 2 of the Compton cross section of water from the NIST database. Indeed, the Klein-Nishina formula intensively used in this context actually introduces inaccuracies at low energies, typically when $E \leq 20\ keV$. We paid a particular attention to the photoelectric component, which offers more contrast between objects than the Compton component or any other classical microCT reconstructed image.

To do this, we have simulated analytically a cylinder of one material (adipose tissue or soft tissue as defined by *ICRP*) inserted in a cylinder of water. We processed photoelectric and Compton separation on projections and computed contrast on reconstructed slices defined as

$$\frac{|S_{mat} - S_{water}|}{S_{mat} + S_{water}}$$

between material and water. In this case, separation is processed from two acquisitions obtained by a modulation of spectrum (W target) by changing filters ($150\ \mu m$ Cu and $25\ \mu m$ Nb).

To measure noise generated by separation, we computed *contrast to noise ratio* (CNR) defined by

$$\frac{|S_{mat} - S_{water}|}{\sqrt{\sigma^2_{mat} + \sigma^2_{water}}}$$

between material and water. Values are reported in Table I. Values of CNR and contrast estimated on the photoelectric component show the relevancy of this approach when comparing these to the CNR and contrast on two reconstructed slices from data simulated with two different filters, i.e. with $150\ \mu m$ Cu and $25\ \mu m$ Nb. For both materials, CNR and contrast against water were increased with the estimation of the photoelectric component.

	Adipose + Water			Soft Tissue + Water		
	Nb	Cu	ph.	Nb	Cu	ph.
CNR	11.2	12.0	23.3	2.03	1.55	4.02
Contrast	0.16	0.11	0.30	0.05	0.03	0.03

Table I: Results of CNR and contrast computed for two different phantoms on ML-EM reconstructed slices of data simulated with a $25\ \mu m$ Nb filter, a $150\ \mu m$ Cu filter, and from the photoelectric component after photoelectric/Compton separation.

B. Beam hardening reduction

Because the photoelectric and Compton components are defined to be energy independent, we are also able to reduce beam hardening. We illustrate this point on Figures 3 and 4, for which we simulated tomography acquisitions of high contrasted objects (Aluminum balls in water) in order to generate beam hardening. After a ML-EM reconstruction of data acquired with Aluminium or Niobium filtration, beam hardening can be observed within and between the Aluminium balls. On the contrary, almost no beam hardening is visible on the reconstruction processed from the photoelectric component. In this case we used a spectrum generated by a Mo target and the component separation was processed by modulating the spectrum with 3 filters ($2\ mm$ Al, $25\ \mu m$ Nb, $150\ \mu m$ Cu).

On Figure 4, we can see an almost flat profile between the Aluminium balls on the reconstruction of the photoelectric component, whereas the profiles of balls on other reconstructions decrease at the center of the balls, which reveals beam hardening. Moreover, the linear attenuation coefficient between the Al balls in the water cylinder reconstructed without component separation appears clearly underestimated, whereas this signature of beam hardening is hardly visible after component separation in the water cylinder.

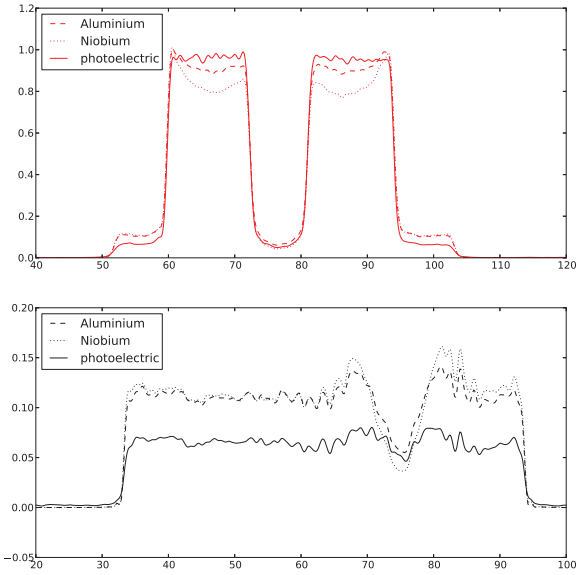

Figure 4: Profiles along colored paths drawn in Fig. 3. Beam-hardening effect is canceled on the component a_{ph}.

C. Results on real data

We have performed real acquisitions with PIXSCAN of the object displayed on Figure 5. The imaged object is composed of an eppendorf filled in with an Yttrium solution at $50\ mg/mL$ concentration and a $0.5\ mm$ thick Aluminium disk. Both objects are immersed in water. Yttrium has a K-edge value of $17\ \ keV$ and is treated as a contrast agent.

For this experiment, we seek to estimate three different components of the scene, namely the photoelectric, Compton

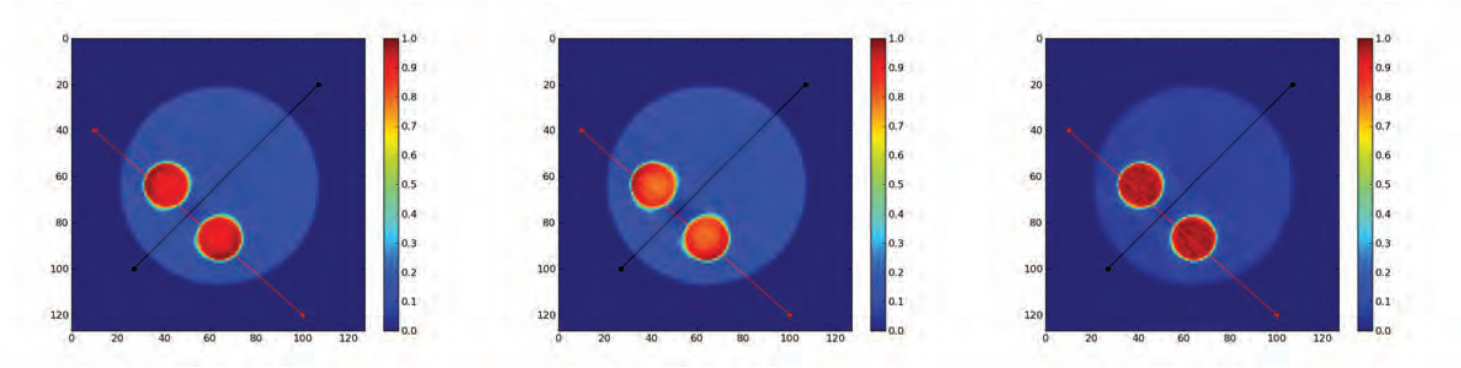

(a) (b) (c)

Figure 3: ML-EM reconstructions of a cylindrical phantom of water with two Aluminium balls in water processed from: a) acquisitions behind a 2 mm Al filter; b) acquisitions behind a 25 μm Nb filter; c) the photoelectric contribution after component separation from 3a, 3b and a third acquisition behind a 150 μm Cu filter. The beam-hardening effect is visible on 3a and 3b whereas it is canceled on 3c. For comparison purpose, reconstructions have been normalized in the range using a Hounsfield unit.

and Yttrium contributions so that $K = 3$ in Equation 1 with $a_3 = a_Y$ and $\mu_Y(E)$ set to the linear attenuation coefficient of Yttrium as described in the NIST/XCOM database. The separation process takes as an input four acquisitions performed using 3 different filters (25 μm Ag, 25 μm Nb and 100 μm Cu) and an unfiltered acquisition, so that $N = 4$ in Equation 1.

On the results displayed on Figure 6, we observe that the Aluminium disk is uniform in the photoelectric and the Compton components with stronger photoelectric contribution in the Aluminium disk than in water and weaker Compton contribution in the Aluminium disk than in water. The chip structure of the detector (right-left effect) appears in both contributions with a stronger impact on photoelectric component because of tiny calibration differences that are not yet considered in the algorithm. On the Yttrium contribution, only the Yttrium contained in the eppendorf appears as expected. All the other pixels in this component have values equal to 0 or close to 0.

V. Conclusion

We have proven that the spectral decomposition of an object in the photoelectric, Compton and K-edge components can be realized with the microCT demonstrator PIXSCAN. Work is being carried on to get a spectral tomography for the localization and and quantification of contrast agents by their K-edge values with photoelectric and Compton component separation within the rest of the acquisition scene.

References

[1] R.E. Alvarez and A. Macovski, *Energy-selective reconstructions in X-ray computerised tomography*, Phys. Med. Biol., 21 (1976) 733-744.

[2] E. Roessl, *Sensitivity of photon-counting based K-edge imaging in X-ray computed tomography*, IEEE Trans. Med. Imaging, 30 (2011) 1678-1690.

[3] P. Delpierre, *PIXSCAN : Pixel detector CT-scanner for small animal imaging,*, Nucl. Instrum. and Meth. , A 571 (2007) 425-428.

[4] P. Pangaud, *XPAD3 : a new photon counting chip for X-ray CT-scanner*, Nucl. Instrum. and Meth., A 571 (2007) 321-324.

[5] F. Cassol Brunner et al., *Imaging performance of hybrid pixel detectors XPAD3-S*, Phys. Med. Biol. 54 (2009) 1773-1789.

[6] H. Ouamara et al., *Comparison of the performance of the photon counting hybrid pixel camera XPAD3 versus the CCD camera DALSA XR-4 for cone-beam micro-CT*, Proc. IEEE NSS/MIC Anaheim, CA, USA (2012) 3756-3759.

[7] F. Cassol Brunner et al., *First K-Edge Imaging With a Micro-CT Based on the XPAD3 Hybrid Pixel Detector*, IEEE Trans. in Nucl. Sci. 60 (2013) 103-108.

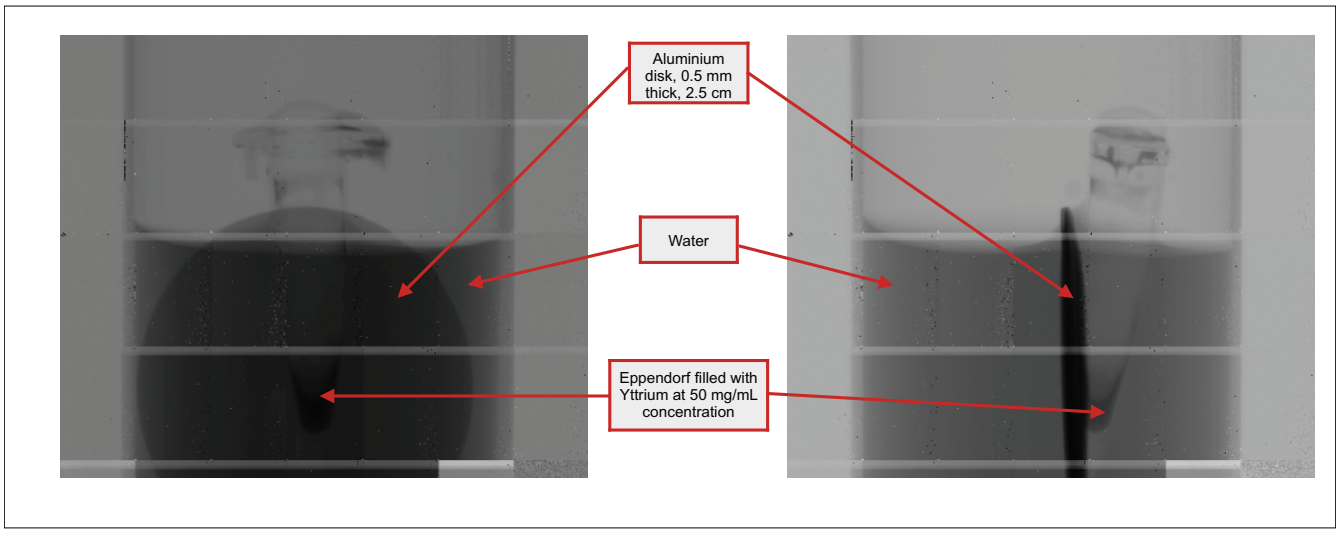

(a) (b)

Figure 5: a) Front view and b) lateral view of the acquisition scene of real data acquired with PIXSCAN. The Aluminium disk and the eppendorf filled with an Yttrium solution are immersed in water.

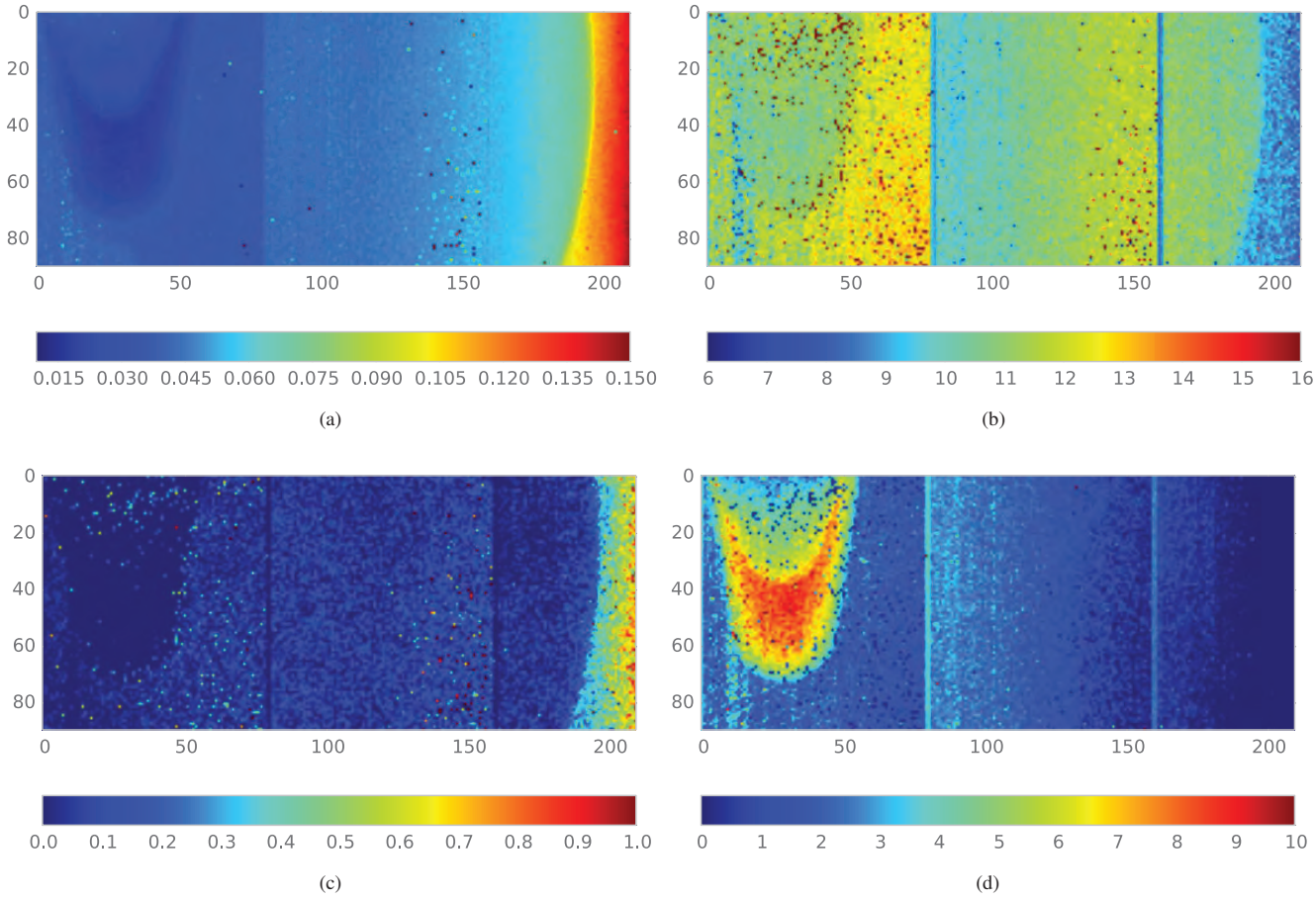

Figure 6: a) Component separation scene (front view) consisting of a (27×12) mm^2 window set across the Aluminium disk edge and the eppendorf observed with 25 μm Nb filtering. Results of the component separation from 4 different acquisitions for the b) photoelectric, c) Compton and d) Yttrium components.